ANL/NE-15/37

Max Data Report

Jet Stability versus Inlet Geometry

Nuclear Engineering Division

About Argonne National Laboratory
Argonne is a U.S. Department of Energy laboratory managed by UChicago Argonne, LLC under contract DE-AC02-06CH11357. The Laboratory's main facility is outside Chicago, at 9700 South Cass Avenue, Argonne, Illinois 60439. For information about Argonne and its pioneering science and technology programs, see www.anl.gov.

DOCUMENT AVAILABILITY

Online Access: U.S. Department of Energy (DOE) reports produced after 1991 and a growing number of pre-1991 documents are available free via DOE's SciTech Connect (http://www.osti.gov/scitech/)

Reports not in digital format may be purchased by the public from the National Technical Information Service (NTIS):
U.S. Department of Commerce
National Technical Information Service
5301 Shawnee Rd
Alexandria, VA 22312
www.ntis.gov
Phone: (800) 553-NTIS (6847) or (703) 605-6000
Fax: (703) 605-6900
Email: **orders@ntis.gov**

Reports not in digital format are available to DOE and DOE contractors from the Office of Scientific and Technical Information (OSTI):
U.S. Department of Energy
Office of Scientific and Technical Information
P.O. Box 62
Oak Ridge, TN 37831-0062
www.osti.gov
Phone: (865) 576-8401
Fax: (865) 576-5728
Email: **reports@osti.gov**

Disclaimer
This report was prepared as an account of work sponsored by an agency of the United States Government. Neither the United States Government nor any agency thereof, nor UChicago Argonne, LLC, nor any of their employees or officers, makes any warranty, express or implied, or assumes any legal liability or responsibility for the accuracy, completeness, or usefulness of any information, apparatus, product, or process disclosed, or represents that its use would not infringe privately owned rights. Reference herein to any specific commercial product, process, or service by trade name, trademark, manufacturer, or otherwise, does not necessarily constitute or imply its endorsement, recommendation, or favoring by the United States Government or any agency thereof. The views and opinions of document authors expressed herein do not necessarily state or reflect those of the United States Government or any agency thereof, Argonne National Laboratory, or UChicago Argonne, LLC.

ANL/NE-15/37

Max Data Report

Jet Stability versus Inlet Geometry

prepared by
S. Lomperski and N. Bremer
Nuclear Engineering Division, Argonne National Laboratory

September 2015

Rev. 0

CONTENTS

Summary 1

1. Introduction 2
1.1 Background 2

2. Data layout 3
2.1 PIV data planes 3
2.2 Inlet conditions 5

3. Test campaign overview 5
3.1 Lid flow field 5
3.2 Inlet flow field 6

4. Test results 7
4.1 Lid flow patterns at Re=10000 7
4.2 Pattern consistency at Re=18000 10
4.3 Mismatched jet flow rates 11
4.4 Mismatched jet temperatures 12
4.5 Inlet flow field maps for matched jets 12
4.5 Velocity 15mm above inlets for matched jets 15

Appendix A *Facility description* 18
Appendix B *Sample flow and temperature data for Reynolds 10000* 23
Appendix C *Instrument accuracy and calibration schedule* 27

Summary

This document describes experiments investigating the effect of inlet geometry on the flow field within a glass tank where two jets mix and impinge upon the lid. The setup mimics the outlet plenum of a fast reactor where core exit flows of different temperatures can mix in ways that induce thermal cycling in neighboring structures.

Two geometries were tested: 1) the "extended" case where hexagonal inlet channels protrude into the tank, and 2) the "flush" case without protrusions. Jets were matched in flow rate and temperature so that channel length is the sole difference between cases.

Flow fields above the inlets and beneath the lid were mapped with particle image velocimetry for inlet Reynolds numbers of 10000 and 18000. The essence of the results is captured by the images below showing typical lid flow field data. Orientation of the data plane is horizontal and so the viewpoint is from above the tank looking down onto the inlets. The contour represents mean velocity magnitude, averaged over 200 s, with the black spots denoting zero. The three spots in the extended case indicate stable jets while the single spot for the flush case is a product of instability. Testing over a range of inlet flow rates and temperatures indicates the difference in stability is due solely to the geometry change.

The new data serves as a challenging benchmark to validate turbulence models in the context of thermal striping and general turbulent flow mixing. This work is a prelude to nonisothermal testing involving thermal mixing and buoyancy-induced flows for a closer parallel to thermal striping applications.

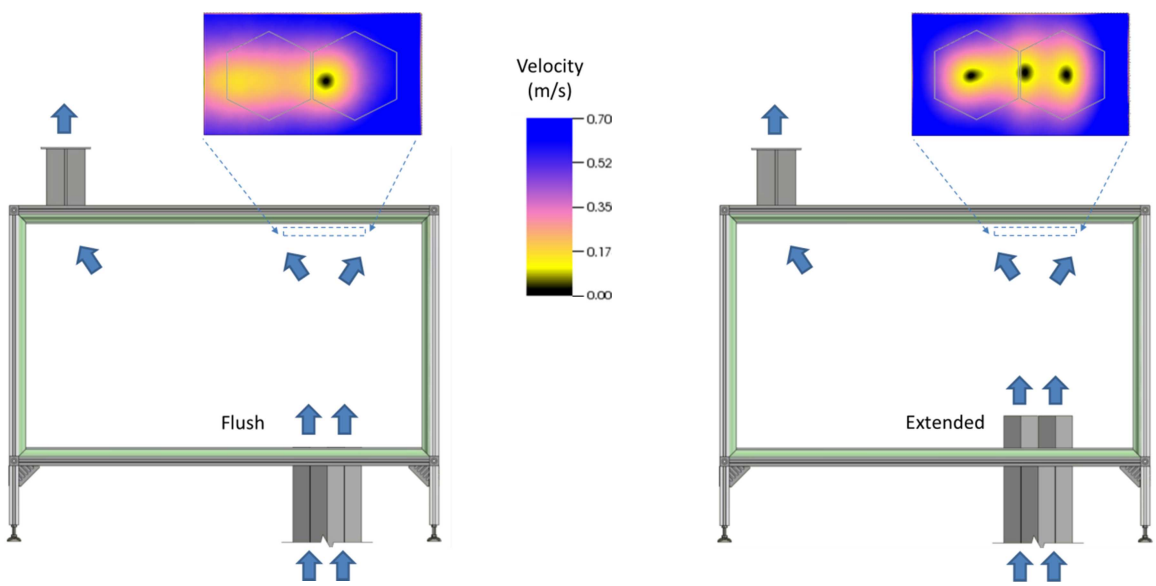

1. Introduction

DOE-NE is developing integrated multi-physics simulation tools for design and analysis of advanced nuclear power systems. Part of this effort involves generating experimental data to validate computational fluid dynamics (CFD) codes specifically for nuclear applications. The Max facility at Argonne National Laboratory is involved in this effort through the NEAMS (Nuclear Engineering Advanced Modeling and Simulation) program. The facility targets turbulent mixing phenomena that can be found in both sodium and gas-cooled reactors. The current configuration mimics an outlet plenum where core exit flows of different temperatures can mix to induce unwanted thermal cycling on neighboring structures (Fig. 1). Extreme cases can lead to component failure through thermal fatigue. This report describes a series of Max tests where minor changes in geometry are seen to profoundly alter this sort of jet mixing flow field. The data provides a straightforward and challenging case for CFD code validation in the context of thermal striping.

1.1 Background

CFD can simulate complex, multidimensional flow fields with high spatial and temporal resolution to provide valuable insights that are inaccessible through traditional lumped parameter codes. Supercomputers paired with sophisticated, high-fidelity CFD codes can now simulate in detail even the complex flows found in nuclear systems. However, such simulations are expensive, lengthy, and generally confined to a small portion of the system of interest. Engineers and designers needing faster and cheaper solutions will typically use lower-fidelity codes run on conventional computing systems. Since code alternatives offer a spectrum of resolution, accuracy, and physical modelling capabilities, analysts try to maximize efficiency by matching the job with the appropriate tool to obtain an adequate level of detail and accuracy with minimum resource expenditure.

What is the best tool for the job? What will provide a sufficiently realistic and accurate representation of the flow field for the task at hand? Guidance can be provided through benchmarks comparing a full spectrum of simulation methods to experimental data. The most faithful reproductions of a flow field would be expected from high-fidelity codes. Detail is progressively lost as one moves along the spectrum towards lower order codes and models. This type of benchmarking highlights the abilities and limits of each tool along the fidelity spectrum.

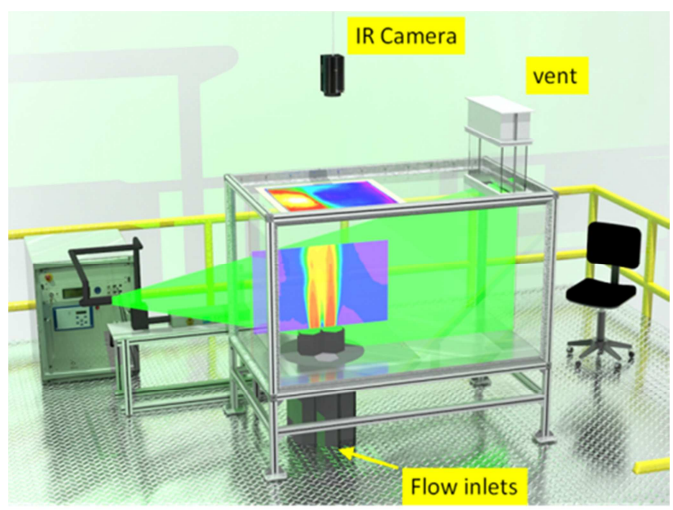

Fig. 1. Setup for thermal striping experiments. Two jets enter glass tank through hexagonal channels at base. Vertical contour shows velocity data, horizontal shows lid temperature data from infrared camera.

Low order tools can be benchmarked by high fidelity tools, which in turn are validated through high-resolution, multiscale experimental data. Such data is generally obtained using unconventional measurement techniques involving lasers and cameras. Unfortunately, optical instruments are not well suited for flow systems at high temperature and pressure, and are useless with opaque fluids. Though the nuclear

systems of ultimate interest here do indeed involve opaque, high-temperature working fluids, the Max facility operates with air near ambient conditions to achieve optimum performance from its collection of optical instrumentation. The strategy maximizes spatial and temporal resolution of the validation data, which is essential in characterizing multiple flow scales.

Fortunately, prototypical fluids are unnecessary for this sort of validation, which checks how well simulations duplicate the physics embodied in the Navier-Stokes equations. The basic physics of thermal striping are the same for liquid metals and transparent fluids like air, but only with the latter can we generate multiscale data to validate high-fidelity simulations.

This report describes a series of tests with the Max facility investigating the subtle effects of inlet geometry on the tank flow field. Two cases were tested: 1) the "extended" case where hexagonal inlet channels protrude 136 mm into the tank, and 2) the "flush" case without protrusions (Fig. 2). Jets were matched in flow and temperature at ambient temperature and pressure with channel length as the sole difference between cases. Isothermal testing avoids the complexities of buoyancy-induced secondary flows while serving as a prelude to the nonisothermal tests that will better parallel the thermal striping applications of ultimate interest.

2. Data layout

2.1 PIV data planes

Flow fields at the inlet and beneath the lid were measured with particle image velocimetry (PIV). This report focuses on the lid flow field as the response quantity of interest, but extensive measurements were also collected at the inlet to characterize boundary conditions. This section describes orientation and location of the data planes. Detailed descriptions of the test section and instrumentation are included as a report appendix.

The lid flow field was measured by orienting the laser sheet in the horizontal direction as shown in Fig. 3. This configuration measures only velocity components in the horizontal plane, not in the vertical direction towards the lid. The light sheet was positioned as close as possible to the lid surface with the understanding that the vertical velocity component there is negligible.

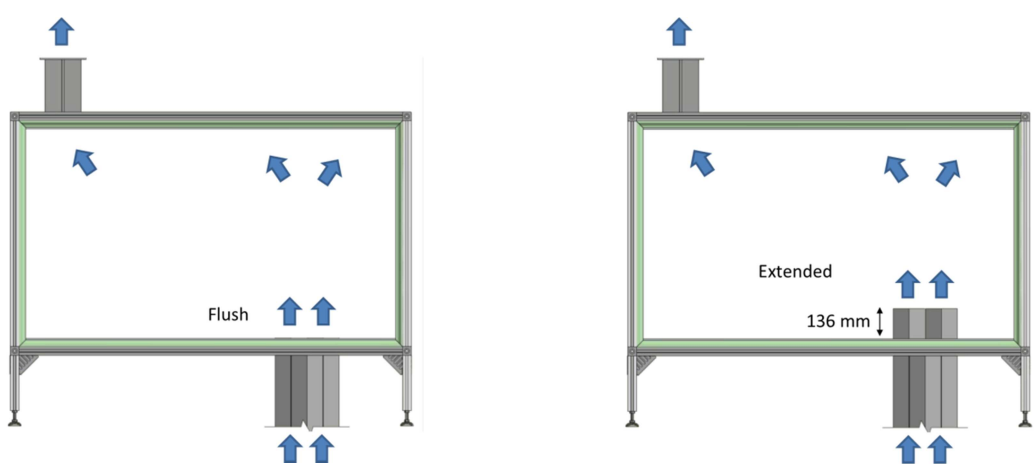

Fig. 2. Test geometries for the flush and extended cases.

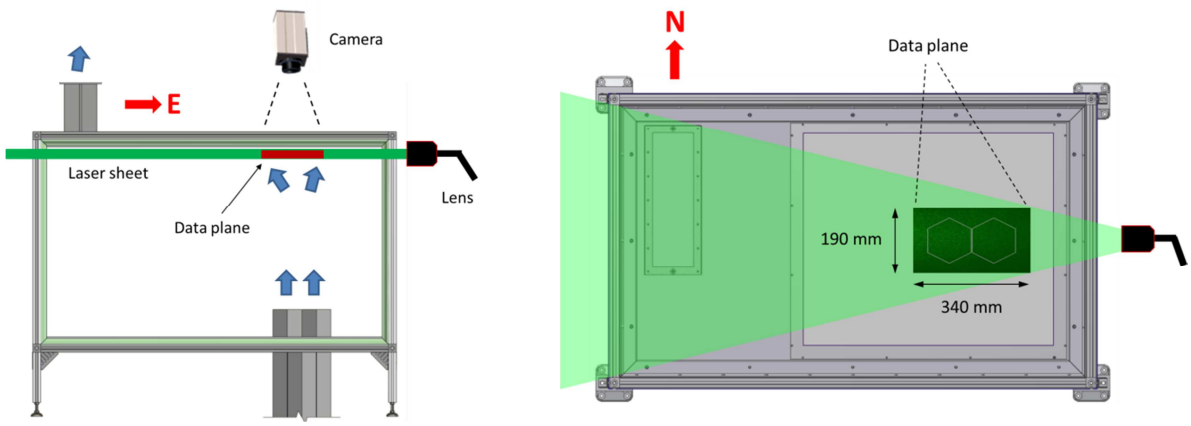

Fig. 3. PIV setup for lid flow field measurements. Laser sheet located ~3 mm below the lid. Dimensions shown for data plane are typical.

Laser sheet thickness was ~2 mm with the center located ~3 mm below the lid surface. Uncertainty in both these parameters is approximately ±1 mm due largely to uncertainties in sheet angle (not perfectly parallel with plane of lid) and sheet focus (thickness varies with distance from lens with a minimum around the data plane for maximum intensity).

A data plane is delimited by the camera field of view (FOV), which in most cases was roughly 340 x 190 mm. A data plane contains 119 x 66 vectors at a spatial resolution of 2.9 x 2.9 mm. Each data plane is derived from a series of 1000 image pairs logged at 5 Hz over a period of 200 s. All velocity data presented here is based on an average of such a series.

Inlet velocity was mapped with PIV at the locations shown in Fig. 4. The wide view image shows the position of inlet data planes relative to the lid data plane, which is 943 mm above the tank base. The accompanying close-up emphasizes the discrete nature of the flow mapping. Data planes are oriented in the vertical direction rather than horizontally across the inlets. The main direction of the flow should

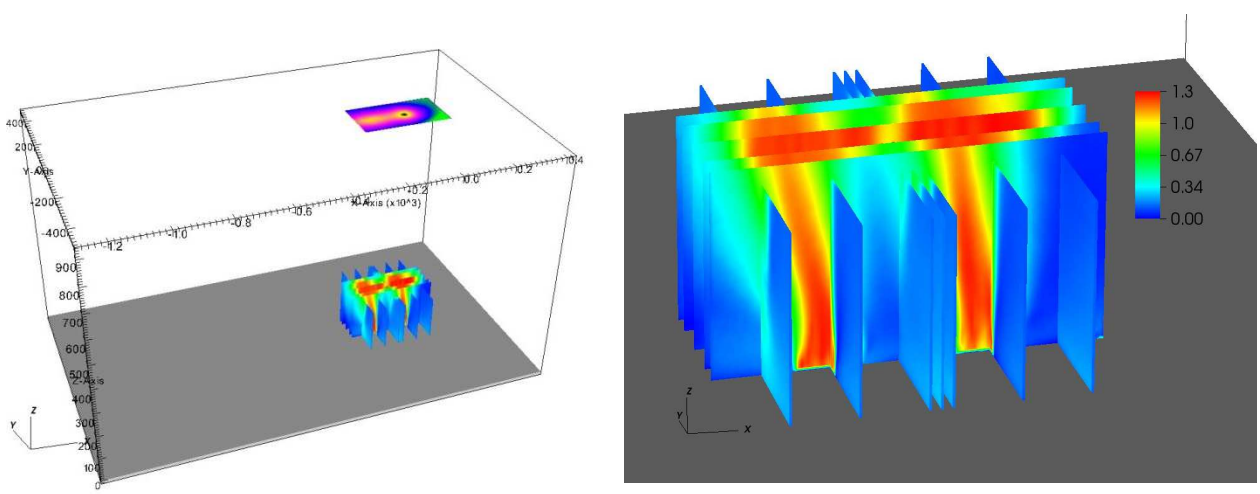

Fig. 4. Data plane locations for inlet velocity mapping with PIV. Left: wide view including lid data plane; right: close-up of data for flush case. Contours indicate velocity magnitude in m/s.

not be through the light sheet because PIV performs poorly with high velocities perpendicular to the light sheet.

The flow field was measured at selected locations in the N/S and E/W directions to characterize all three velocity components. The flush and extended cases are each mapped with the same number of planes, but at different elevations to accommodate the presence or absence of the extensions. In both cases the bottom of the data plane is a few millimeters above the end of the channels.

2.2 Inlet conditions

Boundary conditions were measured by a collection of temperature and flow sensors logged by LabVIEW at 1 Hz. Appendix B provides a sample data set recorded during lid PIV measurements at Reynolds 10000. Tabulated values are based on 200 s averages of data logged while recording a PIV data set. The recording periods for the LabVIEW and PIV data are matched no better than ±60 s because the two systems were not synchronized and PIV start times were noted only to the nearest minute. But this is sufficient since all measurements were made for steady state conditions. System stability can be judged from the tabulated data by examining both variance in the averages and drift between consecutive PIV data sets. Raw data is also available for closer inspection of system conditions.

Inlet and vent temperatures were measured using K-type TCs with an accuracy of ±2.2 ^{o}C for absolute temperature and ±0.1 ^{o}C for differential temperature. The ΔT between the inlets is known to within ±0.1 ^{o}C. Flow is measured by a combination of Coriolis and thermal mass flow meters with the former responsible for more than 97% of the flow. Coriolis meter accuracy is rated at ±0.1% of measured flow, but in-house testing revealed stability errors that are larger because the devices are used at the low end of their measurement range. Zero stability is approximately ±0.1 kg/min, resulting in flow accuracy of ±0.8% for Reynolds 10000 and ±0.4% at Reynolds 18000. Appendix C lists instrument ranges, calibration schedules, and standard accuracies.

3. Test campaign overview

3.1 Lid flow field

The purpose of this study is to generate benchmark data for matched twin jets with two different inlet geometries: flush and extended. The lid flow field was chosen as the response quantity of interest due to its importance in the thermal striping scenario. The test campaign is summarized in bar charts because only a small fraction of the data appears in this report. Data is mostly for Reynolds 10000 since simulations with NEK5000 are more computationally intensive for higher Reynolds numbers.

The isothermal series at Reynolds 10000 consists of 28 1000-frame data sets recorded over two days (Fig. 5). Data sets are split evenly between the flush and extended cases. Testing included flow mismatches up to 10% where one jet is at Reynolds 10000 and the other either 2, 4, or 10% higher, i.e., higher mass flow rate.

Measurements were also made for matched jets at Reynolds 18000 along with mismatches of 2, 5, and 10%. A total of 14 data sets were recorded on a single day, half for the flush case and half for extended.

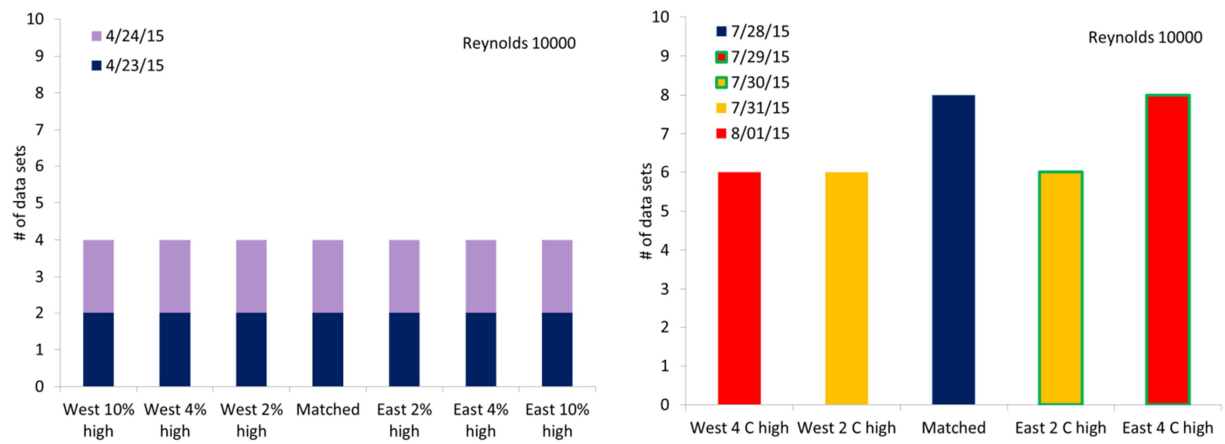

Fig. 5 Data set count for lid flow field measurements at Reynolds 10000 (total of 62). Left: isothermal jets with flow mismatches; right: matched flow rates with temperature mismatches. Sets divided evenly between flush and extended cases.

A follow-up series was conducted for the flush case after observing a potential stability window with mismatched flows. The follow-up was performed for the west inlet high at 2, 4, 5, 6, 7, and 10%.

Though the present study focuses on isothermal mixing, a supplementary test series was conducted with inlet ΔTs of 0, 2, or 4 ^{o}C (Fig. 5). Inlet temperatures were not regulated, but rather one flow stream was heated to achieve the target ΔT. As a result, absolute temperature varied slightly between tests. The facility was run continuously over five days with at least 12 hours of settling time after a temperature change to ensure thermal equilibrium for the measurements.

Ranges for the temperature and flow rate mismatches were chosen to exceed uncertainty bands in the flow meters and thermocouples to ensure that findings are not clouded by questions of whether the jets were truly matched. This will be demonstrated as unimportant since differences in the flush and extended case flow fields are consistent across the investigated range of temperature and flow rate mismatches. Preliminary data analysis indicates that that jet stability is predicted solely by inlet geometry over the entire range of tested conditions.

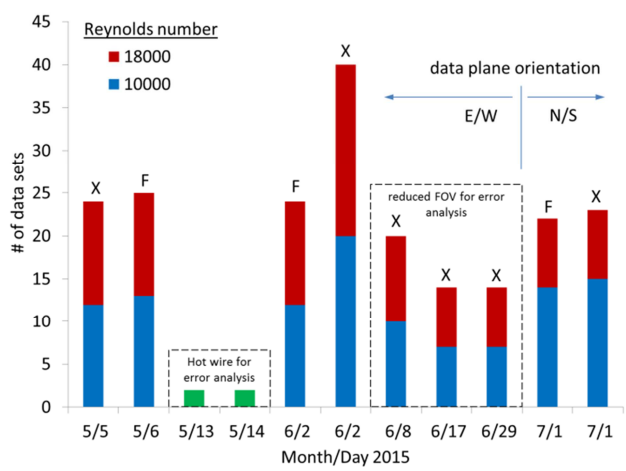

Fig. 6. Data set count for PIV over inlets; flush (F) and extended (X) cases. Hot wire anemometer data at both Reynolds 10000 and 18000, but only extended case along midplane 20 mm above extensions.

3.2 Inlet flow field

Figure 4 above showed the orientation of the PIV data planes at the inlets. Flush planes are located 4 mm above the tank bottom while extended are at 142 mm. East/west oriented planes (long axis of tank) were recorded at 5 positions: centerline and off-center (north and south) ±38 and ±60 mm. North/south oriented planes (short axis of tank) were recorded at 7

positions: middle (between inlets) and off-center (east and west) ±10, ±70, and ±130 mm.

Figure 6 portrays the collection of data sets spanning all combinations of geometry and Reynolds number. The series started with E/W planes for the extended and then flush case with a FOV of 346 x 194 mm followed by two days of point velocity measurements with a hot-wire anemometer for later assessments of PIV accuracy.

The May tests were repeated in June to check for consistency and confirm ability to reproduce system conditions. They included supplementary measurements with the extended case at ±1 and ±2 mm off-center to assess errors associated with positioning uncertainties. A total of 113 E/W data sets were recorded at a FOV of 346 x 194 mm.

Three days were spent measuring with a reduced FOV for later assessments of PIV accuracy. The FOV on 6/8 was 181 x 102 mm, and on both 6/17 and 6/29 it was 70 x 39 mm. Laser pulse frequency was also varied for later error analysis. A total of 48 east/west planes were recorded solely for error analysis. Note also that the smaller FOV is expected to provide more accurate measurements of RMS.

In July the camera and laser were repositioned for measurements in the N/S direction. Measurements were made for both geometries and Reynolds numbers on a single day. This is the only set of N/S planes since the setup was not revisited later to characterize repeatability. A total of 45 N/S data sets were recorded, 29 at Reynolds 10000 and 16 at Reynolds 18000.

4. Test results

Results are condensed into a collection of color contour plots and line graphs describing basic flow field properties for the flush and extended cases. All data presented here is based on averages of 1000-frame image series recorded over 200 s. The raw data is available for more detailed analysis such as power spectrum calculations and proper orthogonal decomposition.

Data has been selected to highlight differences between the two cases and support the notion that jets are stable in the extended case but unstable for the flush case. Speculation on the physics underlying the difference is beyond the scope of this report. And identifying the root cause of the observed behavior may require new measurements in unexplored regions of the tank. Such activities should be guided by analysts since they can more easily explore the flow domain through simulation results.

4.1 Lid flow patterns at Re=10000

Figure 7 presents flow velocity across the lid for inlet Reynolds number 10000. All contours are from the matched data set recorded on April 23rd. Figure 7a shows velocity magnitude V_{mag}, i.e., $\sqrt{u^2+v^2}$. Outlines of the hexagonal channels are overlaid onto the contours as an orientation aid. The view is from above the tank down onto the lid with the tank outlet at the northwest corner. The coordinate system origin is centered between the two inlets at the tank midline with velocity components towards the north and east defined as positive. Cardinal points are used here as a convenience that simplifies plot descriptions in the text. The east wall is at +434 mm and the west wall at -1300 mm.

FLUSH **EXTENDED**

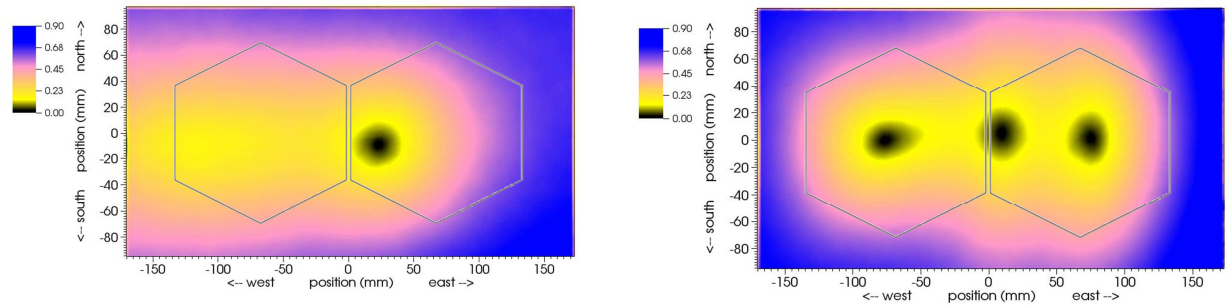

a) Velocity magnitude $V_{mag} = \sqrt{u^2 + v^2}$

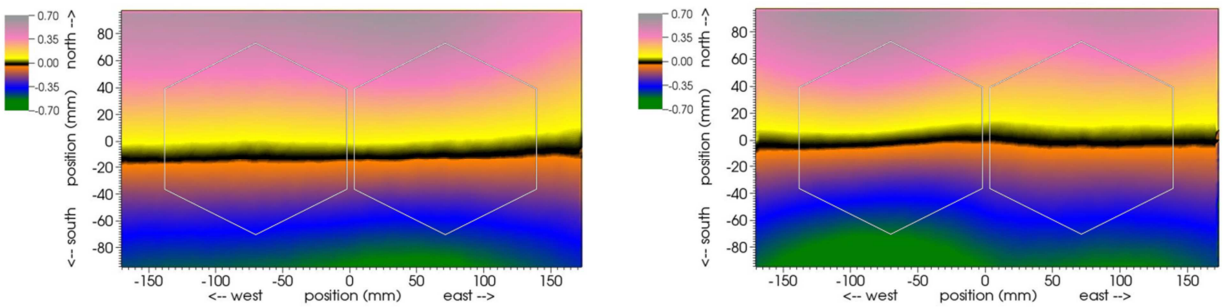

b) N/S velocity component; northward defined as positive.

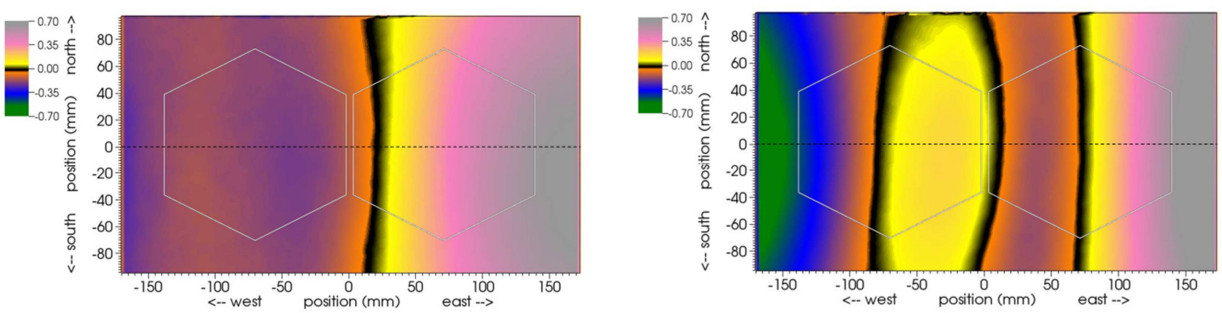

c) E/W velocity component; eastward defined as positive; dashes show sample line for plots in Fig.10.

Fig. 7. Velocity field ~3 mm below lid for matched jets at Reynolds 10000. All velocities in m/s.

The black spots in Fig. 7a mark regions where the time-averaged flow is near zero. These are denoted as "stagnant" regions for brevity even though instantaneous velocity is generally nonzero. They are considered stagnant in the sense of zero mean velocity within a stationary flow field. Viewed in this fashion, the extended case exhibits three stagnant spots and the flush case only one.

Distinctions between the two cases are highlighted by decomposing velocity into E/W and N/S components (Fig. 7b-c). The N/S components are similar in each case, both with a stagnant band roughly centered over the inlets and nearly parallel to the tank's E/W axis. Each band marks the region where the jets split into northward and southward flows that travel across the lid towards opposing walls. Neither case displays exceptional symmetry, but recall that the outlet is located off-axis and so genuine symmetry is not expected. Indeed, the vent was intentionally positioned off-axis to avoid symmetries that could cause random cycling of the flow field between mirror-image states.

In contrast to the N/S velocity component, the E/W component differs markedly between flush and extended cases (Fig. 7c). The latter shows three stagnant bands and the former only one. Note the correspondence between stagnant bands and spots with each band having a counterpart spot. These patterns are emblematic of the disparity between the flush and extended case flow fields, and they persist between repeated measurements on the same day as well as different days.

Though the time-averaged data reveals pronounced differences in the stationary flow field associated with the inlet geometry, it does not indicate whether dynamic characteristics of the flow field also differ. Stability is examined here by plotting RMS (root mean square, standard deviation) of the N/S and E/W velocity components (Fig. 8). A new color palette is introduced to clearly distinguish RMS data from the time-averaged velocities of the preceding plots. Figure 8a shows relatively uniform N/S RMS in the extended case while the flush case is nonuniform with a high intensity region over the east inlet. A clear disparity is also evident in the E/W component. The extended case has a concentrated band of relatively high RMS centered between the inlets while the flush case is far more diffuse with the region of highest intensity located above the west jet rather than centered.

This collection of data suggests jet stability in the extended case and instability in the flush case. In the extended case, RMS is low everywhere except the interface between the jets where shear flows and mixing generate extra turbulence. The high RMS region is narrow because the interface is stable, indicating the jets themselves are stable. Stability is also indicated by the three stagnant spots in Fig 7a, which are consistent with jets rising straight up from the inlets to spread across the lid in a symmetric fashion. Such a flow pattern would generate a stagnation point directly above each inlet. A third

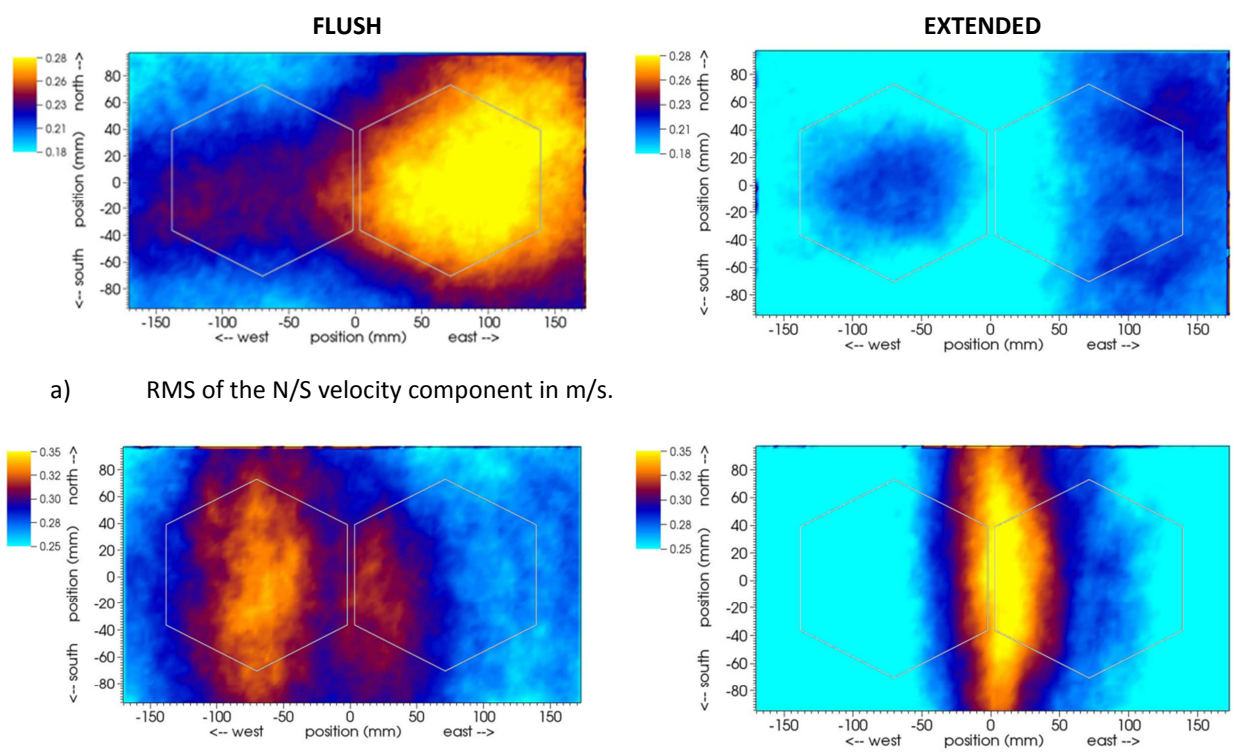

a) RMS of the N/S velocity component in m/s.

b) RMS of the E/W velocity component in m/s.

Fig. 8. Velocity RMS ~3 mm below lid for matched jets at Reynolds 10000.

stagnation point would exist at the symmetry point where the two spreading flow fields meet. The same symmetries generate the stagnant bands of Fig 7c.

The flush case is markedly less stable. The RMS plots indicate strong N/S fluctuations of the east jet accompanied by weak fluctuations of the west jet, and just the opposite for the E/W RMS component. The west jet moves in the E/W direction while the east jet moves in the N/S direction, being stable in the E/W direction because it is pinned between the east wall and west jet. Recall that the east wall is only 434 mm from the centerline while the west wall is 1300 mm away.

4.2 Pattern consistency at Re=18000

The flow patterns observed for an inlet Reynolds number of 10000 are also see at Reynolds 18000. Figure 9 shows a reduced set of velocity and RMS data at Reynolds 18000 to highlight the similarities.

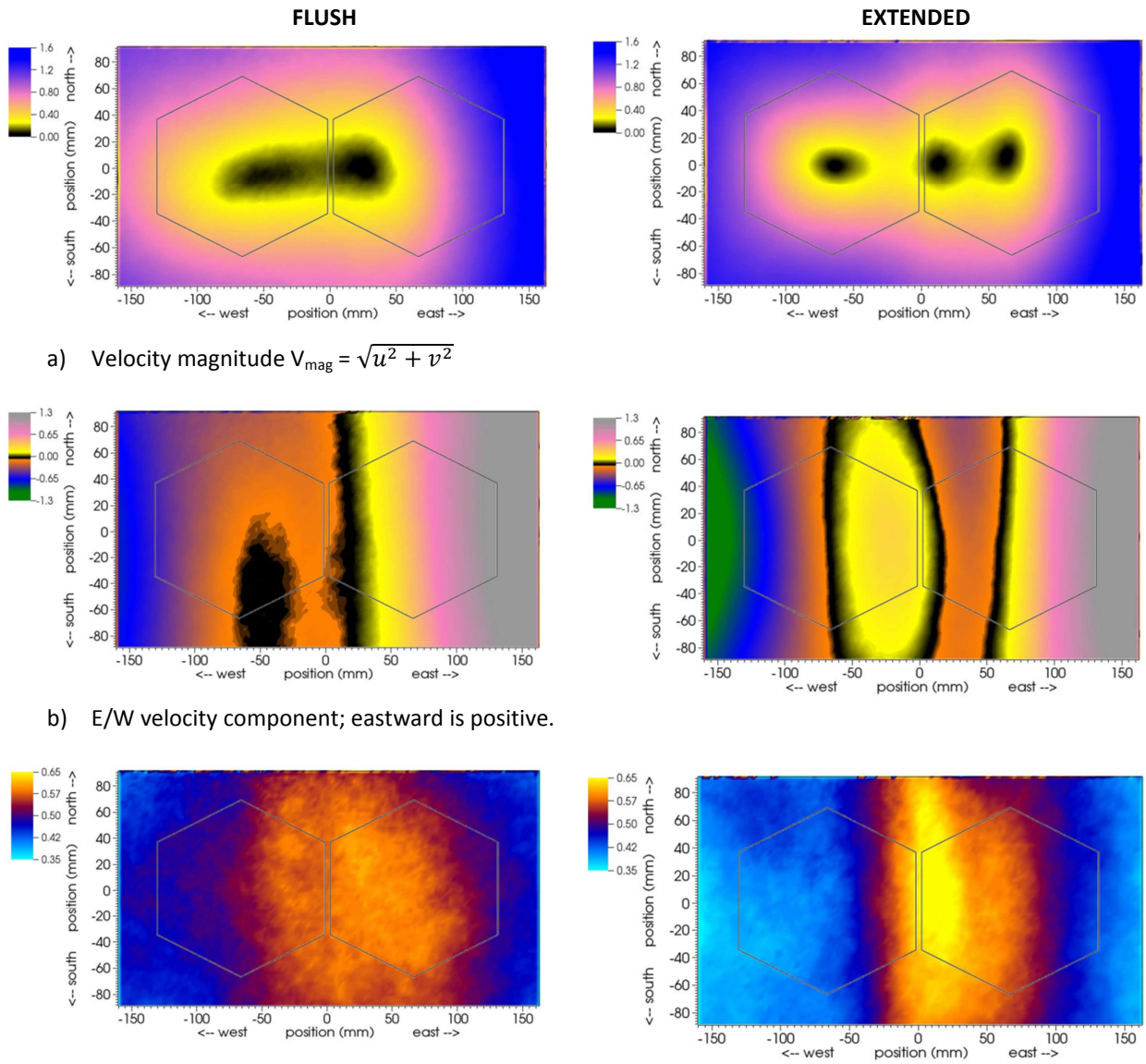

a) Velocity magnitude $V_{mag} = \sqrt{u^2 + v^2}$

b) E/W velocity component; eastward is positive.

c) RMS of the E/W velocity component.

Fig. 9. Velocity and RMS ~3 mm below lid for matched jets at Reynolds 18000. All velocities in m/s.

The extended case again exhibits three stagnant spots in the plot of velocity magnitude with corresponding bands in the E/W component. The flush case also echoes the pattern at Reynolds 10000, but with an extra stagnant region over the west inlet and the beginnings of a second stagnant band in the E/W component. The RMS patterns are also repeated with a relatively sharp band for the extended case and more diffuse distribution for the flush case. In both cases RMS at 18000 is much higher than at Reynolds 10000, as expected.

4.3 Mismatched jet flow rates

Tests again involved isothermal conditions, but with one jet at Reynolds 10000 and the other 2, 4 or 10% higher. The east jet is high for half the tests while the west jet is high for the other half. Two tests were run with matched jets for a comparison baseline. The purpose here is to exclude the possibility that the pattern switch occurs only for precisely matched flow rates, or for mismatched flows mistakenly thought to be matched due to measurement uncertainty. If patterns are consistent across a range of inlet flow rates, it will support the case that variations are due solely to the geometry change.

Figure 10 shows the E/W velocity component below the lid along the tank centerline. PIV data was sampled along the dashed line shown in Fig. 7c. The effective line width is 3 mm, the size of a PIV interrogation area. Each curve is an average of two 1000-frame image series, one recorded on 4/23 and the other on 4/24.

For each geometry, the collection of curves has a distinctive shape that is maintained despite flow rate variations. All flush case data exhibits a single zero crossing while the

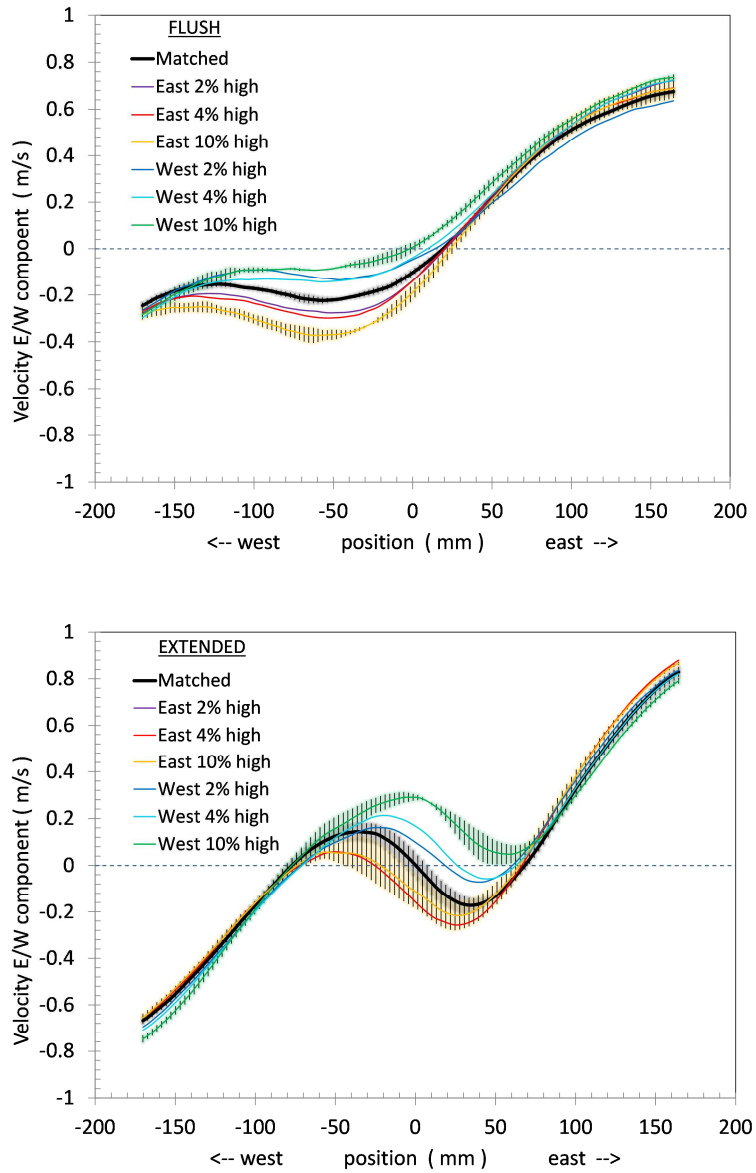

Fig. 10. Velocity below lid along centerline for flow mismatches (sample line shown in Fig. 7c); shaded regions represent ±σ based on measurements from two different days (for clarity plotted only for matched and ±10%). Note that σ varies with position.

extended case curves cross zero three times for all flow combinations except west 10% high. Zero crossings coincide with the black bands of E/W velocity described earlier. Shifts in the velocity profiles are orderly and consistent across the spectrum of flow mismatches: curves shift downward with east jet increases and upward with west jet increases. Note that the most significant profile shifts occur near the inflection points.

Error bands are based on the standard deviation of the sample used to calculate the plotted average. Despite the small sample size, only two for each flow rate combination, the standard deviation is a useful indicator of uncertainty because measurements were recorded on two different days. It is likely to provide a better indication of uncertainty than more numerous records logged on a single day.

Standard deviation was computed as a function of position, showing that variability between tests is generally greatest near the inflection points. Despite the small number of samples and substantial σ, the data suggests that flow mismatches up to 10% generate regular, repeatable shifts in the E/W velocity component along the lid centerline.

4.4 Mismatched jet temperatures

A final set of tests explored the influence of mismatched jet temperatures on the lid flow field. Tests again involved both the flush and extended configurations near Reynolds 10000, but with a ΔT of 4, 2, or 0 ^{o}C at the inlets. The purpose is analogous to that of the mismatched flow rate series, to confirm persistence of the flow patterns over an inlet temperature mismatch range that exceeds measurement uncertainty (ΔT accuracy better than ±0.1 ^{o}C). These tests also offer an opportunity to search for a threshold where buoyancy-induced flows begin to have a discernible influence on lid flow patterns.

Final results are not presented here since an informal blind benchmark is still in progress. But we note that orderly shifts are observed with a ΔT as small as 2 ^{o}C, suggesting that buoyancy-induced secondary flows have perceptible effects even at rather low ΔT.

4.5 Inlet flow field maps for matched jets

Over two hundred 1000-frame image series have been recorded above the inlets. Many parameters were varied: Reynolds number, inlet geometry, camera field of view, data plane orientation, data plane height, and laser pulse rate. We include here a small data subset to provide a general sense of the inlet flow fields, limiting it to Reynolds 10000 and the largest fields of view.

Figure 11 shows velocity fields across E/W-oriented planes positioned directly above the inlets. Contours indicate velocity magnitude $V_{mag}= \sqrt{u^2 + v^2}$. Keep in mind that the flow maps in each case are at different elevations: the bottom edge of flush contours are at y= 4 mm while the extended contours are at y= 142 mm. They look similar, however, because both are positioned a few millimeters above the end of the channels where flow enters the tank proper.

In both cases, the jet cores project directly upward, but the edges at ± 60 mm are skewed towards the west and the vent on the northwest corner. The effect is most pronounced in the flush case, which also has higher RMS along the shear regions around the outside edges of the jets (not shown).

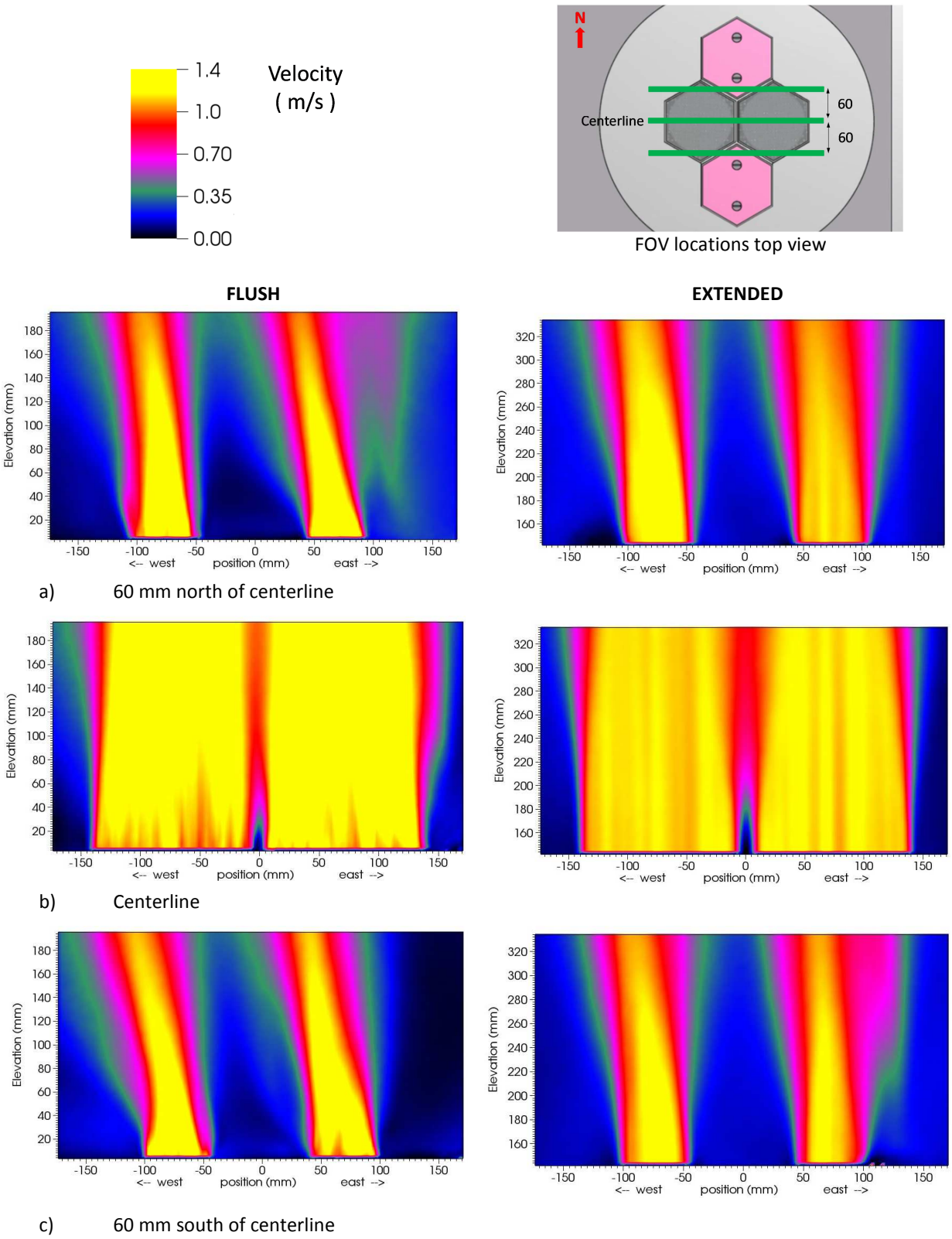

Fig. 11. Velocity magnitude $V_{mag}=\sqrt{u^2+v^2}$. for Reynolds 10000. Vertical data planes oriented in the E/W direction. Note data plane for extended case is 138 mm higher than flush case.

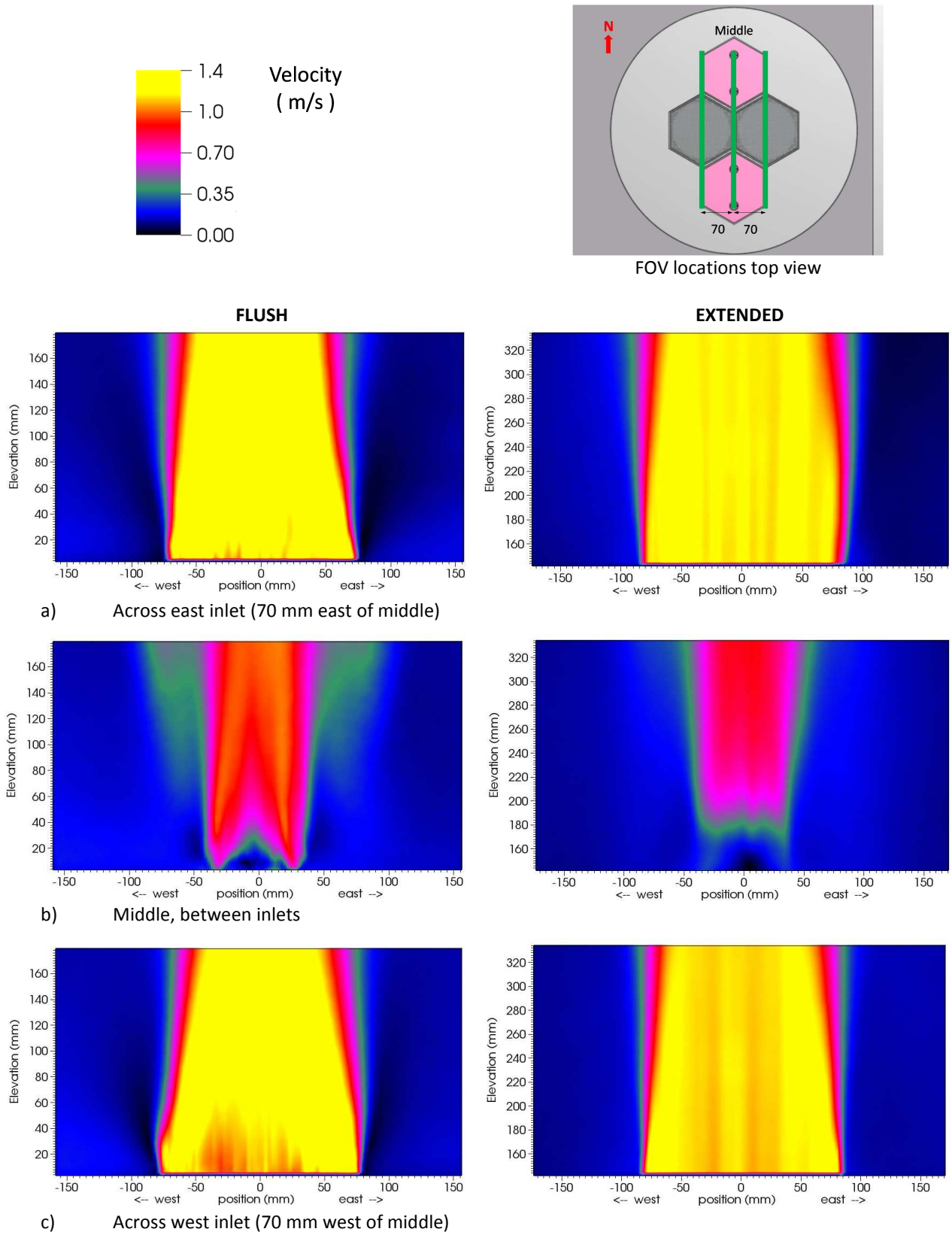

Fig. 12. Velocity magnitude $V_{mag}=\sqrt{u^2+v^2}$. for Reynolds 10000. Vertical data planes oriented in the N/S direction. Note data plane for extended case is 139 mm higher than flush case.

Figure 12 provides data planes in the N/S direction, which are again at different elevations in each case. The flush case exhibits a noticeable narrowing of the jet near the top while the extended case is less constricted. More notable is the symmetry in both cases with no skew towards the north or south. This is consistent with the observed lid flow field and its even split towards north and south directly above the inlets.

Velocities across the middle plane (Fig. 12b) are relatively low, demonstrating that the jet cores are not strongly skewed in the E/W direction, which would appear as high velocity where cores cross the middle plane. This is also consistent with the upright orientation of the jet cores seen in Fig. 11b. However, Fig 12b shows evidence of some skewing since velocity across the midplane increases with height. The green halo of elevated velocity in the flush case is lacking in the extended case, again indicating that flush case jets are more skewed.

4.6 Velocity 15 mm above inlets for matched jets

The flow maps presented in the previous section have been sampled to create line plots for a more quantitative view of inlet conditions. Figure 13 shows velocity and RMS data located 15 mm above the inlets, i.e., y= 15 mm for the flush case and y=151 mm for the extended case. We could have chosen sample lines as close as ~8 mm from the inlets, but data quality can be questionable near the edges of the PIV FOV. The selected distance of 15 mm is a compromise that could be optimized with further analysis.

The central feature to note in Fig. 13 is a lack of close correspondence between the two inlet geometries. It is most evident in the RMS data, which is consistently higher for the flush case. The flush configuration also exhibits higher lateral velocities and less symmetric profiles. Differences in symmetry are most easily seen in the vertical velocity component (Fig. 13a). For the extended case, the centerline profile is echoed at ±38 mm. Even at ±60 mm the peak velocities are well matched. But the flush case is far less symmetric, and there is even downward flow between the inlets that is not seen in the extended case.

Figure 14 shows sample lines taken from the N/S data planes of Fig. 12. There is again a poor match between flush and extended cases. Discrepancies in symmetry are most easily seen in the vertical velocity component, most notably the “middle” profile in Fig. 13a. Low vertical velocities are expected along this line of symmetry, but they are observed only in the extended case. The nonzero velocities in the flush case indicate that jet skewing towards the vent begins directly above the inlets. In short, flow fields are quite different at a distance of only 15 mm from the inlets.

This data emphasizes the need to improve characterization of the inlet boundary conditions. Here we have measured above the inlets, which is inside the tank and part of the domain to be simulated. Ideally, however, the flow field inside the channels would be measured, and at a location far enough upstream that the flow field is identical in both the flush and extended cases. One could introduce transparent channels that permit upstream PIV. Design modifications are under consideration.

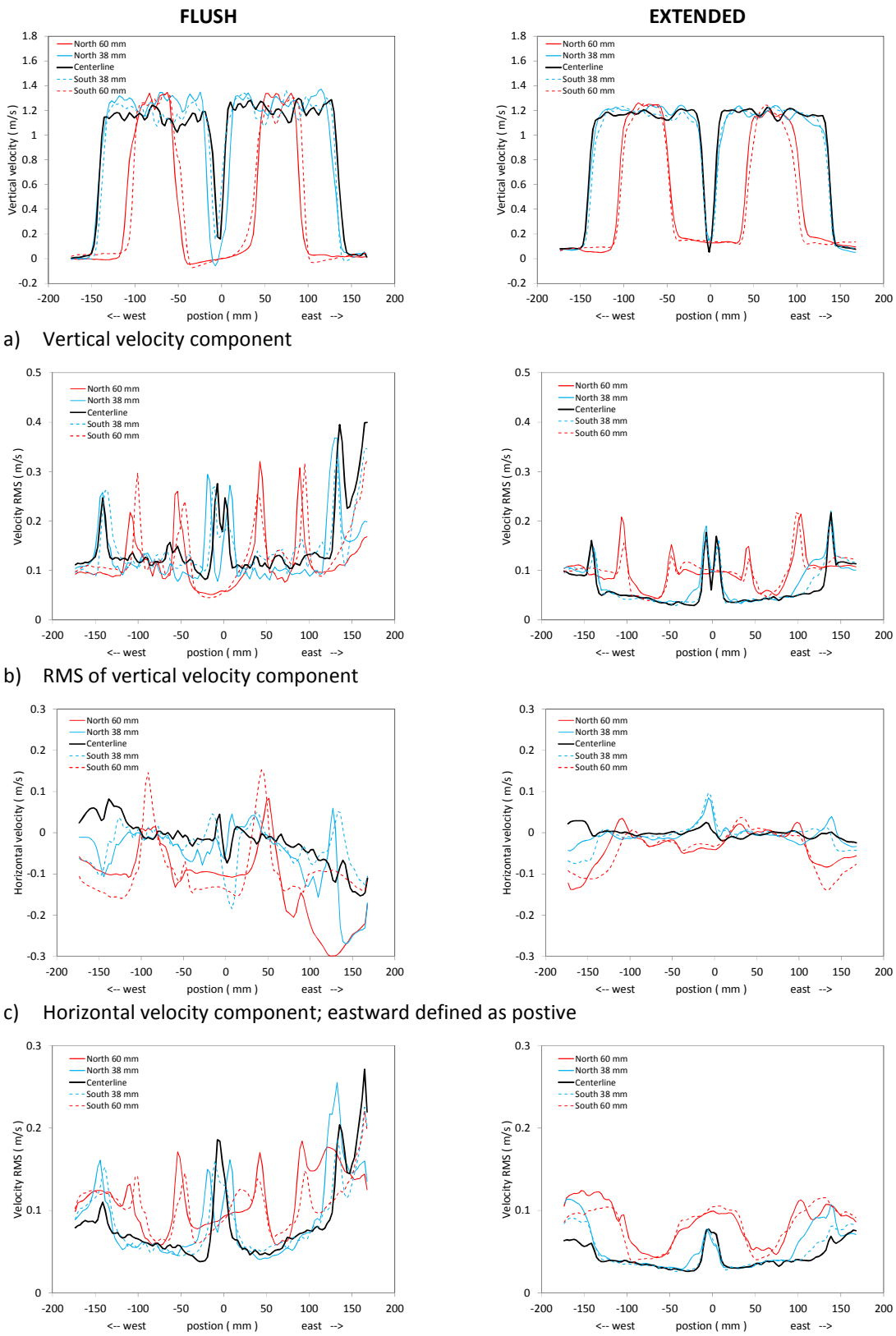

Fig. 13. Velocities over inlets for matched jets at Reynolds 10000. E/W plane data sampled at 15 mm above inlets (y= 15 mm for flush case and y=151 mm for extended case. All velocities in m/s.

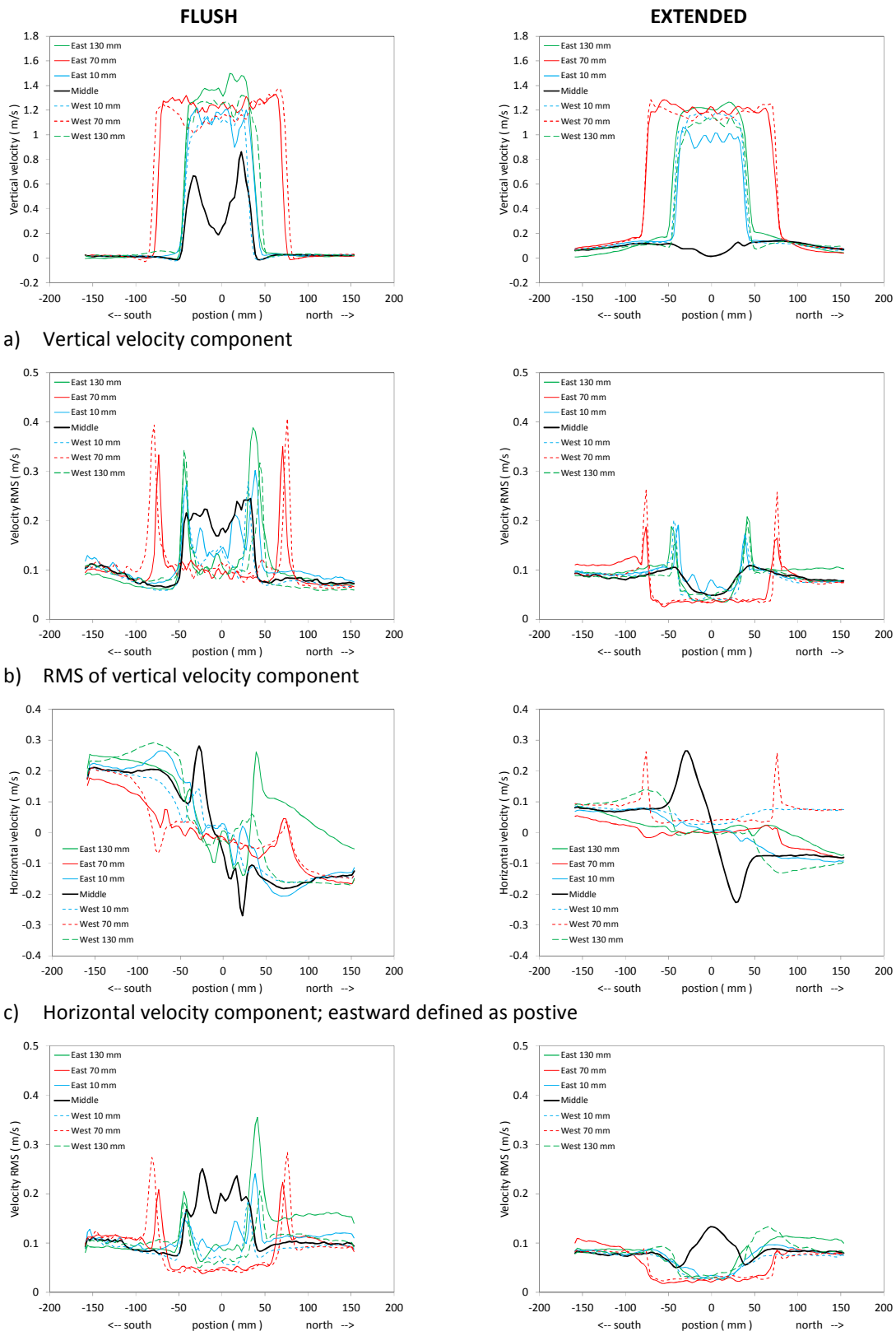

Fig. 14. Velocities over inlets for matched jets at Reynolds 10000. N/S plane data sampled at 15 mm above inlets (y= 15 mm for flush case and y=151 mm for extended case. All velocities in m/s.

Appendix A Facility description

Test section

The jet mixing chamber is a glass tank with inside dimensions of 1.7 x 1 x 0.9 m high, made of 6 mm thick plates (Fig. A.1). The glass is a low-iron soda lime variety with an antireflective coating for maximum light transmission. The outlet duct is 6.5 mm thick Borofloat®33 glass to allow flow mapping in the outlet region. The tank base is 12 mm thick 6061 aluminum with a mill finish. Surface roughness was measured with a portable contact profilometer and found to be in the range of 0.9 -1.1 µm (the glass registered 0.02 µm). The same material was used for the lid and has the same finish and roughness.

An opening in the lid was milled out for a 920 x 778 mm window frame. A thin screen is stretched across the frame for tests involving lid temperature measurements with an infrared camera. For PIV, the window is fitted with a 12 mm-thick transparent polycarbonate plate. The bottom surface of the plate is flush with the underside of the lid.

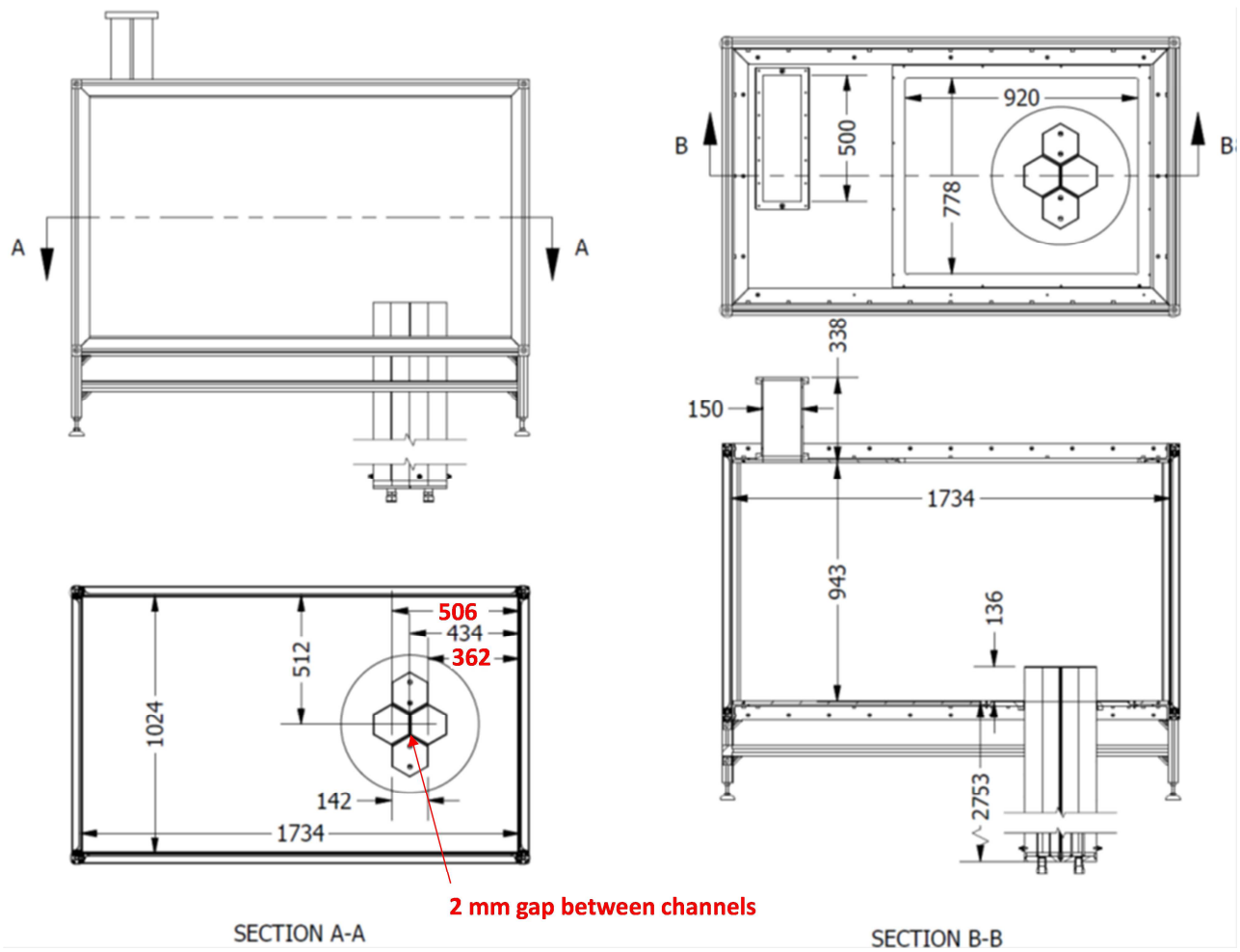

Fig. A.1. Top and section views of test section.

Note that the glass walls do not sit flush against the edges of the base and lid: there is an 8 mm wide x 12 mm deep slot around the edge. The glass sits against an aluminum frame and is sealed round the outside edge by plastic molding. Details are available separately in CAD drawings.

Flow channels

Air flow into the tank is delivered via hexagonal channels having dimensions comparable to those envisioned for recent sodium fast reactor concepts. Channels are extruded aluminum with 3 mm wall thickness, an inside flat-to-flat distance of 136 mm (Fig. A.2), and length of 2.7 m for an L/D of 21. Roughness of the inside surface was measured and found to average ~0.4 µm. Note, however, that this corresponds to clean, as-delivered channel. The channels have become coated with a thin layer of the oil used to seed the flow for the PIV system.

Four channels are mounted to the bottom of the test section with two currently covered with polymer plugs (Fig. A.3). The extensions shown in the photo sit on top of the inlets without glue or sealing compound since they are inserted and removed repeatedly in switches between the flush and extended configurations. The joint is located at the same level as the last mesh and so it should have a negligible influence on the flow profile.

Honeycomb and two layers of mesh were inserted near the outlets to flatten the flow profile. The mesh is woven stainless steel wire ϕ= 0.71 mm, 2.5 mm opening width, and 60.2% open area. The mesh visible in the photo is at the level of the base plate, i.e., 136 mm from the channel end. The honeycomb,

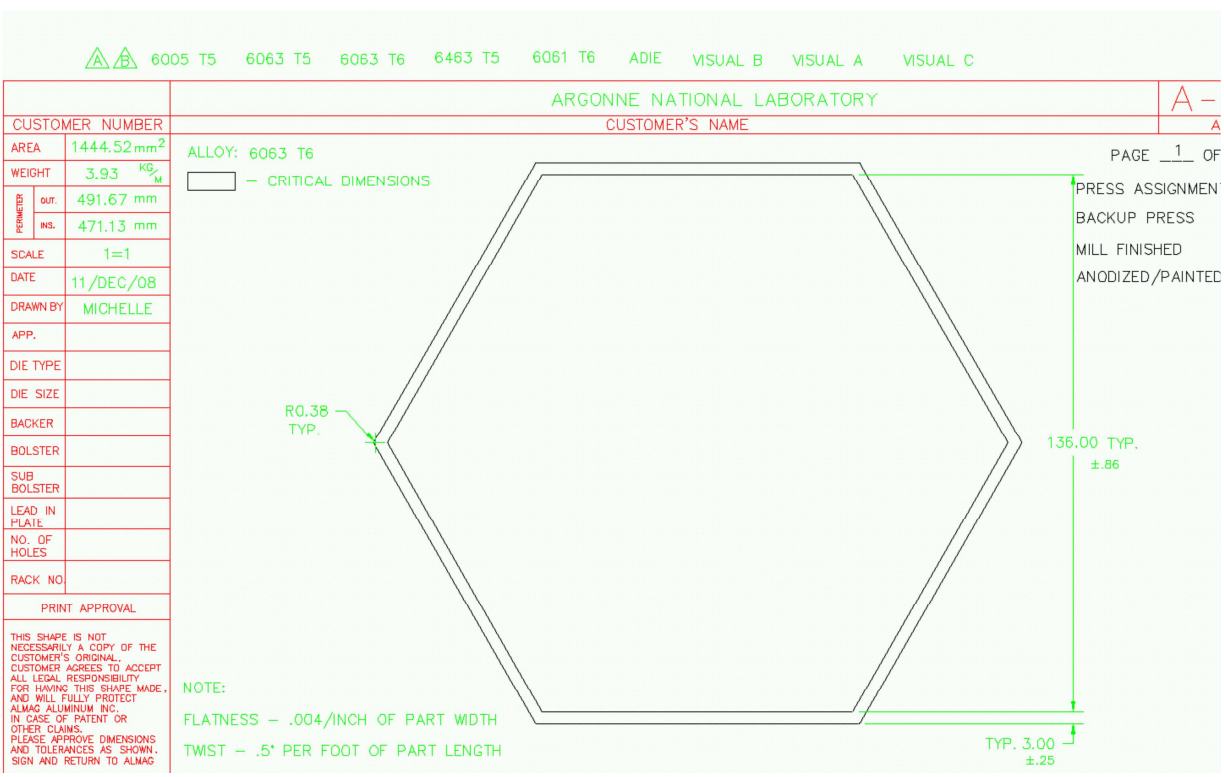

Fig. A.2 Hexagonal channel design detail.

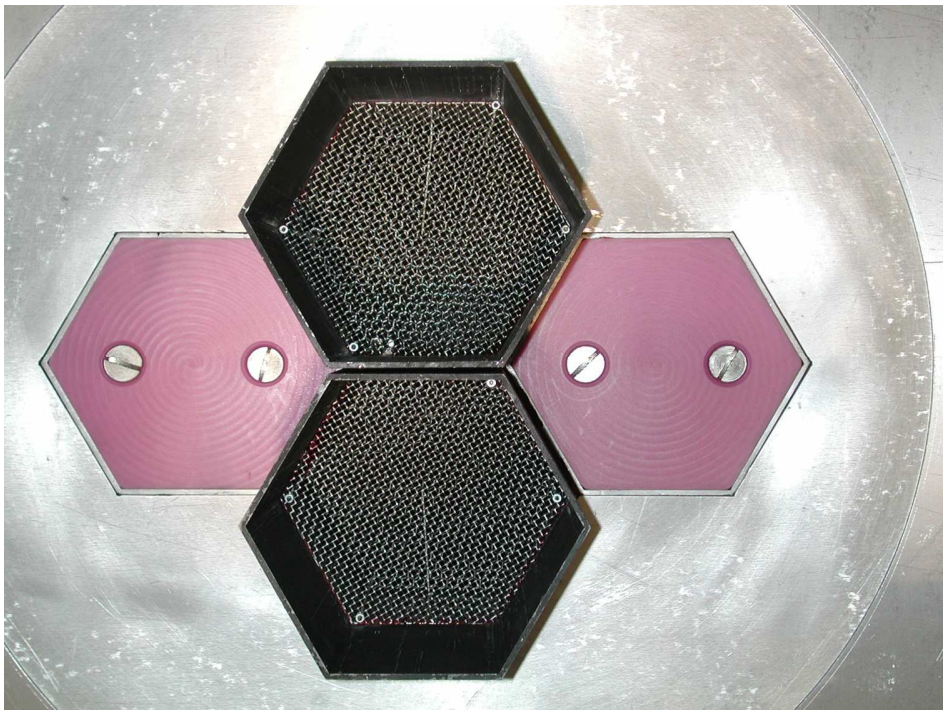

Fig. A.3. Top view of inlets for extended configuration: channels in black with stainless steel mesh for flow conditioning, pink polymer plugs blocking reserve inlets. Air gap between channels is 2 mm (8 mm between inside of flats: 2 mm gap plus 2 x 3 mm wall thickness)

150 mm long with a cell size of 6.4 mm, is 140 mm further upstream. The first mesh is 140 mm upstream of the honeycomb. The inlet conditioning assembly is shown in Fig. A.4.

Flow Seeding

PIV functions by imaging particles in the flow to determine their velocities, which represent in turn the velocity of surrounding fluid. The air was seeded with a mist of propylene glycol, a nontoxic, colorless and odorless organic liquid with a boiling point of 188°C and a vapor pressure <0.1 mm Hg @25°C. A fluid atomizer converts the liquid into a fine mist that is added to the main gas flow. The atomizer generates droplets having an average diameter of ~2 µm. The

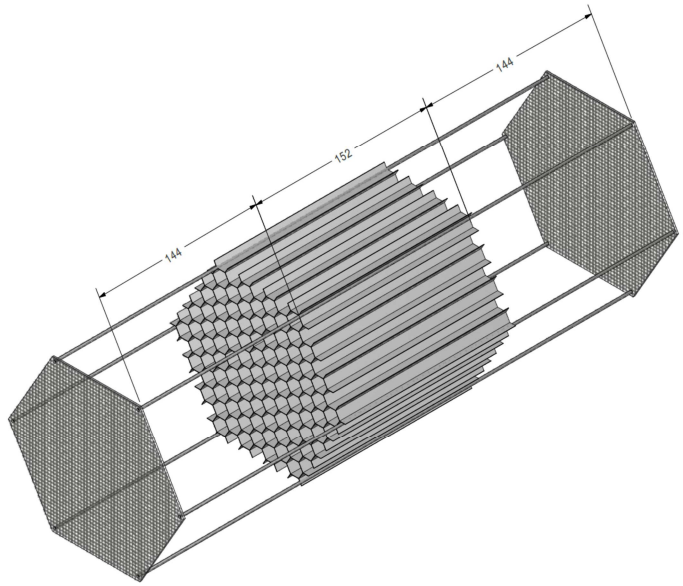

Fig. A.4. Flow conditioning assembly: wire mesh followed by honeycomb and a final sheet of mesh, which is visible in Fig. A.3.

frequency response of these droplets is expected to be ~1 kHz for 2-3 µm droplets and ~10 kHz for those with a diameter ~1 µm, which is sufficient given the bandwidth limit of the PIV system. A HEPA filter atop the exit duct removes seeding particles as air is vented to the room. The pressure drop across the duct elevates the tank pressure to approximately 5 mm H_2O above atmospheric.

Instrumentation

The PIV system uses a Nd:YLF 527 nm (green) dual cavity pulsed laser from Litron Lasers Ltd. The unit is rated for pulse rates up to 10 kHz per cavity and pulse power of 32 mJ for rates below 1 kHz. For this study, the light sheet was generated with a single laser cavity to eliminate alignment errors and sheet thickness was approximately 2 mm. The camera is an IDT model Y7 with a 1920 x 1080 array of 7.24 x 7.24 µm pixels and maximum full resolution speed of 7500 fps. Images were captured using IDT's Motion Studio version 2.10.02. A 50 mm Navitar lens was used at an aperture of 0.96. The typical FOV was roughly 340 x 190 mm for a spatial resolution of about 2.9 mm. Two data sets at reduced FOV were recorded for error analysis: one set at 181 x 102 mm and 1.5 mm spatial resolution and a second at 70 x 39 mm and 0.6 mm resolution. The latter were taken with a 100 mm macro at an aperture of 2.5.

All image processing was performed with Dantec Dynamic's DynamicStudio version 3.31.22. Velocity maps were calculated using adaptive correlation with 32 x 32 pixel interrogation areas, 50% overlap, and subpixel refinement with two refinement steps. Resulting data maps contain 119 x 66 vectors. Data was filtered with a range validation routine and universal outlier detection. Settings vary with Reynolds number and data plane location (lid or inlets), but are stored in the DynamicStudio databases for inspection or new analyses with different settings.

Air feed to the tank is at room temperature and enters the system via two supply lines at the bottom of the hexagonal channel. The main flow is regulated with a Teledyne model 307 flow controller, which also measures the flow rate. A second and more precise measure of flow rate is provided by an Endress & Hauser model 83F coriolis flow meter to an accuracy of ±0.1 kg/min. The seeding flow is measured with a Teledyne model 301 thermal mass flow meter within ±0.4 lpm. The main flow oscillates ±3 lpm around the setpoint with a period of 10 s due to feedback between the flow controller and the compressor supplying air to the facility. Channel flow is conditioned with honeycomb and mesh inserts at the upstream end of the channels where the main and seeding flows mix, and by the mesh and honeycomb near the tank inlet described earlier.

Inlet temperatures are measured with thermocouples located 100 mm below the tank base. Gauge pressure at the same location is measured by pressure Setra pressure transmitters having a frequency response >100 Hz. The pressure difference between the two channels is also measured. Both the pressure and temperature signals are filtered with 4 Hz cutoff frequency and data is logged at 1 Hz.

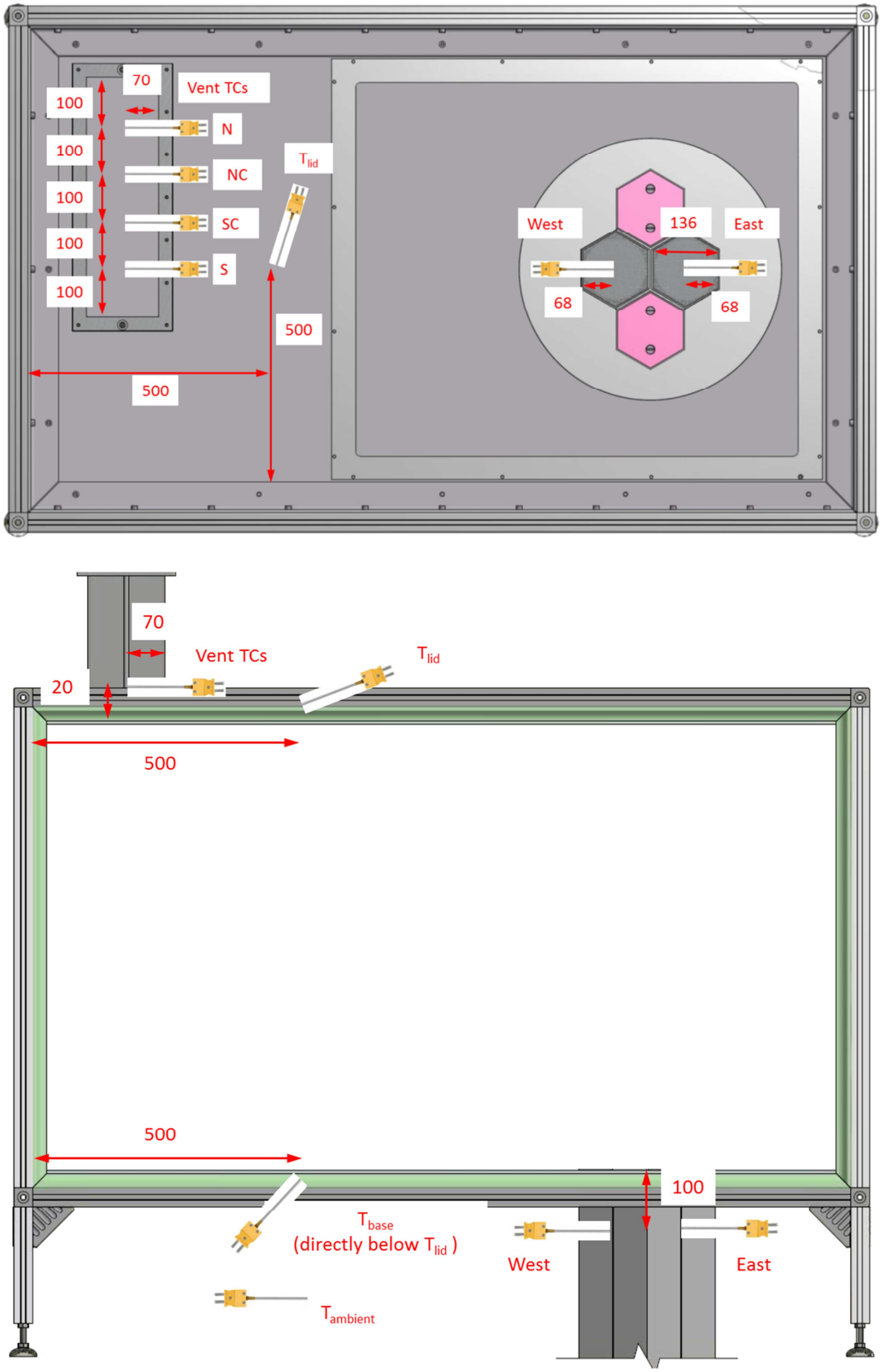

Fig. A.5. Thermocouple locations. Dimensions in mm.

Appendix B: Sample flow and temperature data for lid PIV at Reynolds 10000

Table 1 of 4: Flow rates

	Date	PIV start time	Image series name	Flow East (kg/min)	σ (kg/min)	Flow West (kg/min)	σ (kg/min)	Re # East	Re # West
1	4/23/15	17:27	Extended matched 1	1.254	0.006	1.246	0.005	10020	9955
2	4/23/15	17:47	Extended matched 2	1.254	0.006	1.245	0.006	10021	9951
3	4/23/15	17:57	Ext. east 2% high	1.276	0.006	1.246	0.005	10195	9953
4	4/23/15	18:08	Ext. east 4% high	1.300	0.006	1.246	0.005	10390	9952
5	4/23/15	18:21	Ext. east 10% high	1.373	0.007	1.245	0.006	10969	9951
6	4/23/15	18:34	Ext. west 2% high	1.254	0.007	1.269	0.005	10018	10139
7	4/23/15	18:47	Ext. west 4% high	1.255	0.006	1.291	0.006	10024	10318
8	4/23/15	19:00	Ext. west 10% high	1.255	0.006	1.361	0.006	10025	10874
9	4/23/15	19:31	Flush matched 1	1.255	0.006	1.247	0.009	10025	9964
10	4/23/15	19:44	Flush matched 2	1.254	0.006	1.247	0.005	10021	9960
11	4/23/15	20:01	Flush east 2% high	1.278	0.006	1.243	0.010	10212	9934
12	4/23/15	20:14	Flush east 4% high	1.303	0.006	1.245	0.005	10408	9951
13	4/23/15	20:28	Flush east 10% high	1.374	0.003	1.246	0.004	10974	9957
14	4/23/15	20:40	Flush west 2% high	1.254	0.006	1.269	0.004	10019	10136
15	4/23/15	20:55	Flush west 4% high	1.254	0.006	1.292	0.005	10020	10327
16	4/23/15	21:08	Flush west 10% high	1.255	0.006	1.361	0.005	10025	10875

Appendix B: Sample flow and temperature data for lid PIV at Reynolds 10000

Table 2 of 4: Temperatures

	Image series name	Inlet East (C)	σ (C)	Inlet West (C)	σ (C)	Lid (C)	σ (C)	Base (C)	σ (C)
1	Extended matched 1	22.85	0.02	22.95	0.02	26.22	0.02	26.38	0.03
2	Extended matched 2	22.84	0.02	22.94	0.02	26.20	0.02	26.37	0.03
3	Ext. east 2% high	22.83	0.02	22.95	0.02	26.18	0.02	26.35	0.03
4	Ext. east 4% high	22.81	0.02	22.95	0.02	26.17	0.02	26.34	0.02
5	Ext. east 10% high	22.77	0.02	22.95	0.02	26.15	0.02	26.32	0.03
6	Ext. west 2% high	22.85	0.02	22.95	0.02	26.14	0.02	26.36	0.03
7	Ext. west 4% high	22.85	0.02	22.93	0.02	26.13	0.02	26.28	0.03
8	Ext. west 10% high	22.85	0.02	22.87	0.02	26.11	0.02	26.32	0.03
9	Flush matched 1	22.85	0.02	22.95	0.02	26.15	0.02	26.38	0.04
10	Flush matched 2	22.85	0.02	22.95	0.02	26.15	0.02	26.37	0.02
11	Flush east 2% high	22.83	0.02	22.95	0.02	26.13	0.02	26.40	0.03
12	Flush east 4% high	22.81	0.02	22.95	0.02	26.12	0.02	26.36	0.03
13	Flush east 10% high	22.77	0.02	22.96	0.02	26.11	0.02	26.39	0.03
14	Flush west 2% high	22.85	0.02	22.95	0.02	26.11	0.02	26.37	0.04
15	Flush west 4% high	22.85	0.02	22.93	0.02	26.11	0.02	26.39	0.05
16	Flush west 10% high	22.85	0.02	22.87	0.02	26.10	0.02	26.41	0.03

Appendix B: Sample flow and temperature data for lid PIV at Reynolds 10000

Table 3 of 4: Temperatures

	Image series name	Vent NC (C)	σ (C)	Vent N (C)	σ (C)	Vent SC (C)	σ (C)	Vent S (C)	σ (C)
1	Extended matched 1	24.87	0.04	24.79	0.05	24.85	0.04	24.79	0.05
2	Extended matched 2	24.86	0.04	24.75	0.04	24.87	0.04	24.81	0.04
3	Ext. east 2% high	24.85	0.04	24.76	0.04	24.84	0.05	24.80	0.04
4	Ext. east 4% high	24.82	0.03	24.73	0.04	24.86	0.04	24.79	0.06
5	Ext. east 10% high	24.81	0.04	24.68	0.04	24.83	0.04	24.76	0.05
6	Ext. west 2% high	24.82	0.04	24.76	0.04	24.78	0.04	24.76	0.05
7	Ext. west 4% high	24.83	0.03	24.73	0.04	24.82	0.06	24.75	0.04
8	Ext. west 10% high	24.78	0.05	24.71	0.03	24.76	0.04	24.76	0.04
9	Flush matched 1	24.83	0.04	24.77	0.03	24.85	0.06	24.83	0.05
10	Flush matched 2	24.83	0.03	24.77	0.04	24.85	0.04	24.83	0.04
11	Flush east 2% high	24.81	0.04	24.72	0.05	24.84	0.04	24.84	0.04
12	Flush east 4% high	24.80	0.04	24.73	0.03	24.82	0.03	24.81	0.05
13	Flush east 10% high	24.78	0.04	24.72	0.03	24.80	0.03	24.78	0.04
14	Flush west 2% high	24.81	0.03	24.73	0.04	24.84	0.04	24.82	0.05
15	Flush west 4% high	24.80	0.03	24.73	0.04	24.84	0.03	24.82	0.04
16	Flush west 10% high	24.76	0.04	24.72	0.04	24.79	0.04	24.81	0.05

Appendix B: Sample flow and temperature data for lid PIV at Reynolds 10000

Table 4 of 4: Temperatures

	Image series name	Ambient (C)	σ (C)	Dewpoint (C)	σ (C)				
1	Extended matched 1	26.92	0.05	-5.3	0.05				
2	Extended matched 2	26.90	0.03	-5.5	0.4				
3	Ext. east 2% high	26.87	0.06	-5.4	0.05				
4	Ext. east 4% high	26.89	0.07	-5.6	0.4				
5	Ext. east 10% high	26.86	0.05	-5.5	0.3				
6	Ext. west 2% high	26.94	0.05	-5.4	0.1				
7	Ext. west 4% high	26.77	0.03	-5.4	0.3				
8	Ext. west 10% high	26.86	0.05	-5.5	0.3				
9	Flush matched 1	26.93	0.09	-5.5	0.3				
10	Flush matched 2	26.92	0.04	-5.5	0.3				
11	Flush east 2% high	26.98	0.06	-5.4	0.3				
12	Flush east 4% high	26.85	0.05	-5.5	0.4				
13	Flush east 10% high	26.95	0.07	-5.4	0.2				
14	Flush west 2% high	26.89	0.06	-5.4	0.2				
15	Flush west 4% high	26.92	0.08	-5.4	0.2				
16	Flush west 10% high	26.93	0.07	-5.4	0.2				

Appendix C: Instrument list

Flow meter	Description	Range	Accuracy	Cal date	Due date
East Controller	Teledyne HFC-D-307 #443360001	0-2500 lpm	±0.5% ±0.2% FS	12/08/14	12/08/15
West Controller	Teledyne HFC-D-307 #443360003	0-2500 lpm	±0.5% ±0.2% FS	11/25/14	11/25/15
East Coriolis	E&H Promass 83F #F4097C16000	0-40 kg/min	±0.1%*	10/24/14	10/24/15
West Coriolis	E&H Promass 83F #F4097D16000	0-40 kg/min	±0.1%*	10/24/14	10/24/15
East Seeding	Teledyne HFM-D-301 #6534000001	0-100 lpm	±0.5% ±0.2% FS	12/05/14	12/05/15
West Seeding	Teledyne HFM-D-301 #5593400001	0-100 lpm	±0.5% ±0.2% FS	12/04/14	12/04/15

Sensor	Description	Range	Accuracy	Cal date	Due date
West Inlet P	Setra C239 #3905749	±15” WC	0.14% FS	04/10/09	-
East Inlet P	Setra C239 #3905750	±15” WC	0.14% FS	04/10/09	-
East/West ΔP	Setra C239 #3905748	±15” WC	0.14% FS	04/10/09	-
Dewpoint meter	GE M2LR #452232-PR	-110 – 20°C	±2 ^{o}C	4/01/14	-

*Zero stability of approximately ±0.1 kg/min observed during in-house testing with flow meters in series.

Nuclear Engineering Division
Argonne National Laboratory
9700 South Cass Avenue
Argonne, IL 60439

www.anl.gov

Argonne National Laboratory is a U.S. Department of Energy
laboratory managed by UChicago Argonne, LLC